

Measurement of the snow accumulation in Antarctica with a neutrino radio detector and extension to the measurement of the index-of-refraction profile

Jakob Beise

Supervisor: Christian Glaser

Examiner: Erin O'Sullivan

Half Time Report - Advanced Physics - Project Course 30 ECTS

Department of Physics and Astronomy - Uppsala University

Friday 12th March, 2021

Abstract

High-energy neutrino physics offers a unique way to investigate the most violent phenomena in our universe. The detection of energies above $E > 10^{17}$ eV is most efficient using the Askaryan effect, where a neutrino-induced particle shower produces coherent radio emission that is detectable with radio antennas. By using radio techniques large volumes can be covered with few stations at moderate cost exploiting the large attenuation length of radio in cold ice. Key to the reconstruction of the neutrino properties is a precise and continuous monitoring of the firm properties. In particular the snow accumulation (changing the absolute depth of the antennas thus the propagation path of the signal) and the index-of-refraction profile are crucial for the neutrino energy and direction reconstruction. This work presents an in-situ calibration design that acts as a detector extension by adding additional emitter antennas to the station design to continuously monitor the firm properties by measuring the direct and reflected signals (D'n'R). In a simulation study the optimal station layout is determined and the achievable precision is quantified. Furthermore 14 months of data from an ARIANNA station at the Ross Ice Shelf, Antarctica, are presented where a prototype of this calibration system has been successfully installed to monitor the snow accumulation with unprecedented precision of 1 mm. Several algorithms, including deep learning algorithms, to compute the D'n'R time difference from radio traces are considered.

Contents

1	Introduction	2
1.1	Optical Neutrino Detectors	2
1.2	Radio Neutrino Detectors	3
1.3	ARIANNA: Antarctic Ross Ice-Shelf ANtenna Neutrino Array	4
1.4	Neutrino Energy Reconstruction	4
2	Snow Accumulation Measurement	7
2.1	Classical Analysis	7
2.2	Deep Learning Analysis	10
3	Simulation of a Detector Extension for the Measurement of Firn Properties	12
3.1	Concept	12
3.2	Results	14
4	Summary and Outlook	16
	References	16

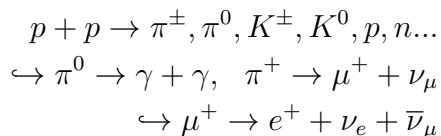
Chapter 1

Introduction

This chapter gives a short introduction to the physical background and motivation for this project work. In Sec. 1.1, the benefits of neutrinos over other messenger particles is covered and the energy limits imposed by optical sensors are discussed. In Sec. 1.2, the strength of radio technology for the high energy spectrum and the general concept of a radio neutrino detector, as well as advantages and disadvantages of different layouts are presented. The current ARIANNA detector station design is described in Sec. 1.3 and a brief overview of the neutrino direction and energy reconstruction performance is given in Sec. 1.4.

1.1 Optical Neutrino Detectors

High-energy (HE) neutrino physics constitutes a unique tool to examine the most violent processes of our universe. Neutrinos offer a way to directly trace back their source of origin at high energies. In contrast, charged cosmic rays whose trajectories are distorted by intergalactic magnetic fields experience a sharp drop in flux beyond 10^{19} eV as predicted by Greisen, Zatsepin and Kuzmin in the GZK-effect. On the other hand, the extragalactic space becomes opaque to photons above 1 PeV due to scattering of high energy photons on the cosmic microwave background radiation (CMB) and extragalactic background light (EBL). There are two mechanisms that can explain the production of HE neutrinos. The astrophysical beam dump,



which describes the collision of two protons p and the subsequent production of charged and neutral mesons that further decay into gamma rays, charged leptons and their neutrino partners, and the photoproduction,

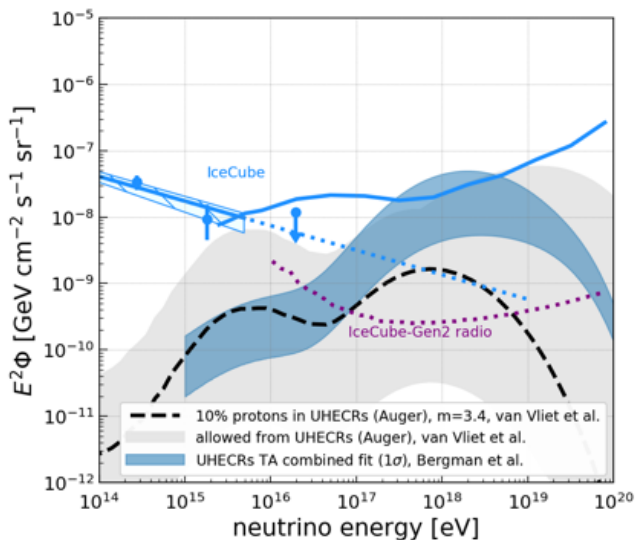
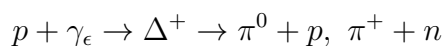


Figure 1.1: Neutrino flux as a function of the neutrino energy. IceCube data is in blue; HE upper limit on the ν -flux by is the solid blue line while the blue dotted line represents the HE extrapolation of IceCube's data. The sensitivity of a future IceCube-Gen2 radio array is in purple. The allowed phase space for ν -flux from measurements by the Pierre Auger Observatory (Telescope Array) is shown as gray band (blue band). A future IceCube-Gen2 radio array would reduce the upper limit of the ν -flux by about $\mathcal{O}(100)$ [1].

representing the collision of an HE proton p with a low-energy, ambient photon γ_e [2]. These production mechanisms point to a strong link between HE cosmic rays, gamma rays and HE neutrinos.

On the downside, neutrinos solely interact weakly and their interaction cross section is comparably small, meaning that a large detection volume is required for a reasonable event rate. The current 1 km^3 IceCube neutrino observatory at the Amundsen-Scott South Pole Station in Antarctica is composed of 5160 optical sensors, so called Digital Optical Modules (DOMs), deployed in ice at depth of 1450 m to 2450 m acting as both the interaction and detection medium. The steady and cool environment represents optimal conditions for a low-noise detector, while the deep deployment of the DOMs combines good ice properties and rejection of atmospheric muons.

A neutrino interacting in the ice causes a particle shower in charged or neutral current interactions. The charged secondaries in turn produce Cherenkov radiation bundled along the Cherenkov cone. The measurement of HE neutrinos is of interest not just for the neutrino flux from $\mathcal{O}(\text{PeV})$ to $\mathcal{O}(\text{EeV})$ but also to reveal the sources and propagation of the highest energy particles and to link it to multi-messengers observations. However, experiments have shown that the neutrino flux decreases with energy and the current IceCube detector runs out of sensitivity for energies above 10^{16} eV (Fig. 1.1). Since scaling the effective detection area up using optical sensors is not cost-efficient, due to the relatively low attenuation length in the optical, an alternative approach is needed [1].

1.2 Radio Neutrino Detectors

Making use of the large radio attenuation length of $\mathcal{O}(1 \text{ km})$ in ice and the comparatively cheap and mature technology, radio neutrino detectors constitute an ideal alternative for the detection of high energy neutrinos. There are two mechanisms that cause radio emission from air showers:

First, the geomagnetic effect, in which charged secondaries in the shower are deflected (or rather accelerated) by Earth's magnetic field emitting electromagnetic radiation in the radio spectrum.

Second, the Askaryan effect that describes how a moving, time-varying charge excess in the electromagnetic component of an air shower, induced by annihilation of positrons and dragging of Compton and δ -electrons from the surrounding air molecules into the shower, acts as a dipole and thus emits short and coherent radio flashes in the frequency range of 50 MHz to 1 GHz. The radio signal is emitted on a narrow cone with an opening angle of 56° , while highest intensity is reached on the Cherenkov cone [3].

Radio neutrino detectors make use of the D'n'R technique (direct and reflected) for the reconstruction of the neutrino vertex distance. This method is based on the unique signature recorded by a $\mathcal{O}(15 \text{ m})$ -deep antenna in the vast majority of neutrino events, consisting of a direct pulse and a slightly delayed signal that is reflected off the ice surface (see Fig. 1.2). Section 1.4 describes this procedure in greater detail and explains how the neutrino vertex

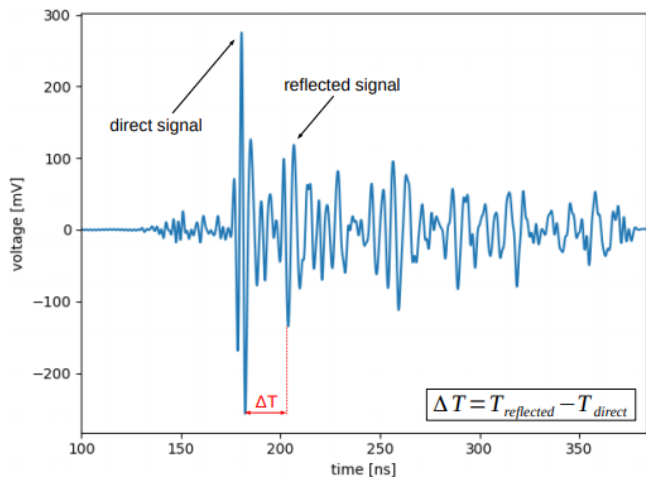


Figure 1.2: D'n'R signal, consisting of the direct and off the surface reflected pulse. The time delay between the former and latter acts as proxy for the neutrino vertex and energy.

distance can be used to infer the neutrino energy. This technique was successfully explored in two pilot projects; ARIANNA at the Ross Ice Shelf and ARA at the South Pole. There is open controversy about the precise layout of a radio detector station.

ARA makes use of dipole antennas deployed in depth of 200 m, thus having a larger sensitivity per station due to the bigger effective volume, because it is less impacted by the firm properties which change drastically between 1.78 for clear deep ice to 1.34 for the surface. However, due to borehole limitations only narrow dipole antennas with a comparatively low gain can be used.

ARIANNA in turn has to deal with the changing index-of-refraction profile that bend the trajectories, reducing the exposure of neutrinos per station and increasing the 'shadow zone' - the spatial region in which the detector is blind because no signals will ever reach it. On the contrary shallow, 3 m deep antennas mean quicker deployment and allow for high-gain, broadband LPDA antennas (log-periodic broadband antenna), that are used to infer the signal polarisation. Additionally a close-to-surface dipole antenna enables to measure the D'n'R signal efficiently. The ARIANNA station is also sensitive to radio signals from cosmic-ray induced air showers which allows for an in-situ calibration and continuous testing of the detector station [4].

1.3 ARIANNA: Antarctic Ross Ice-Shelf ANtenna Neutrino Array

The ARIANNA detector consists of 12 stations successfully operating on the Ross Ice Shelf at Moore's Bay in Antarctica and the South Pole. Each station consists of two pairs of downwards-facing LPDA antennas of orthogonal orientation separated by 6 m (see Fig. 1.3). In a second generation station design two upwards-facing LPDA for cosmic-ray detection and vetoing are complemented.

ARIANNA stations are powered by solar panels during the summer month and in future by wind turbines allowing for operation during the dark winter month. Data is transferred via the Iridium satellite network or high-speed long-range wifi connection, which is susceptible to the weather conditions. The main part of the ARIANNA array consists of seven 4-channel stations, hexagonally arranged at Moore's Bay. Events are triggered using a high and low threshold crossing requirement and coincidence between several channels to reduce the thermal noise trigger rate, resulting in a trigger rate of 10 mHz. An additional trigger to filter out narrowband emissions from ambient sources is applied [4].

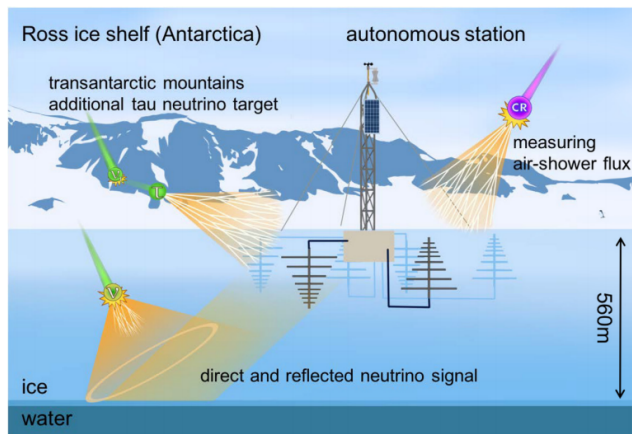


Figure 1.3: Sketch of a the ARIANNA detector station at the Ross Ice Shelf. Figure from [4].

1.4 Neutrino Energy Reconstruction

The aim of radio neutrino detectors like ARIANNA detector is twofold and consists of the measurement of the neutrino flux and point source analysis for HE neutrinos. This section explains how the D'n'R technique can be used to reconstruct the neutrino energy. A summary of the reconstruction procedure and the main results, as described in great detail in [5], is given

in the following. The antenna's radio signal amplitude $\vec{\varepsilon}(f)$ is directly linked to the neutrino energy E_ν by the following, simplified relation

$$\vec{\varepsilon}(f) = \vec{e}_p(\vec{p}, \vec{v}_\nu, \vec{X}_{int}) \times |\vec{\varepsilon}_0(f, E_\nu, y, \dots)| \times \frac{e^{-R/L(f)}}{R} \times \exp\left[\frac{-(\theta - \theta_C)^2}{2\sigma_\theta(f)^2}\right].$$

which consists of four parts: 1) signal direction and polarisation, 2) Askaryan signal, 3) signal attenuation and 4) viewing angle.

The first part describes the polarisation \vec{p} of the Askaryan signal at the detector and takes the neutrino direction v_ν and the position of the neutrino interaction \vec{X}_{int} into account. Second $\vec{\varepsilon}_0$, which incorporates parameters of the neutrino interaction such as the neutrino energy E_ν and the inelasticity y , which imposes an irreducible uncertainty to the measurement. The signal attenuation term is defined by $L(f)$, the frequency depended attenuation length and the vertex distance R . Finally, the viewing angle and the opening angle of the Cherenkov cone θ and θ_C respectively, while σ_θ is the width of the Cherenkov cone. Thus for the reconstruction of the energy E_ν and direction the signal amplitude, the vertex distance, the polarisation and the viewing angle are required.

The radio amplitude scales linearly with the shower energy E_{sh} , which underlies a stochastic process. A key issue is the lack of knowledge whether the interaction is electromagnetically or hadronically induced, which limits the abilities to infer the neutrino energy from the shower energy. Using NuRadioMC [6] for a full Monte Carlo simulation the inelasticity limit is found a factor of two, confining the experimentally achievable energy resolution and setting a bar for the uncertainty of the vertex position and viewing angle, not to further increase the energy resolution beyond that bound.

For the determination of the neutrino vertex position the D'n'R time delay is crucial, complementing radio signal arrival direction and polarisation. Ray tracing is performed using Fermat's least-time principle to infer the neutrino vertex position prescribing the vertex distance. In a simulation vertex positions are randomly placed and the trajectories to a 15 m deep dipole antenna are calculated. Figure 1.4 left shows the time delay as a function of distance for three different incoming directions. As can be seen the D'n'R time difference is inverse-proportional to the vertex distance, as well as the zenith angle θ . The binning of all simulations to 0.1 ns in Δt and 0.1° in θ in dependence of the vertex distance is illustrated in Fig. 1.4 right. This graph can be used to translate time delays and incoming angles into vertex distances.

In order to determine the uncertainty on the neutrino vertex distance, the true zenith angle θ and time difference Δt are smeared 200 times according to a Gaussian distribution of $\sigma_\theta = 0.2^\circ$, $\sigma_{\Delta t} = 0.2$ ns respectively. For 10^{17} eV (10^{18} eV), they find a 68% quantile of 10% (12%). For the uncertainty in the neutrino energy one makes use of $E_{sh} \propto \frac{R}{-R/L}$ resulting in 20% (38%-41%) for 10^{17} eV (10^{18} eV), being significantly smaller than the elasticity limit. Finally, an optimised detector layout featuring a receiver antenna at a depth of -15 m is specified, which is a compromise between the neutrino energy resolution and the efficiency to detect both D'n'R pulses. An investigation of systematic uncertainties yields, that depth of the antenna has to be known to a precision of $\ll 46$ mm to be considered to have an insignificant impact on the energy resolution. Therefore the snow height has to be monitored continuously. Additionally, uncertainties in the index-of-refraction profile $n(z)$ propagate to a systematic uncertainty in the conversion from Δt and zenith angle θ to the vertex distance [4][5]. The next two chapters present results from a functioning calibration device for the snow accumulation measurement (Chap. 2) and a simulation of a detector extension to include firn properties to the calibration(Chap. 3).

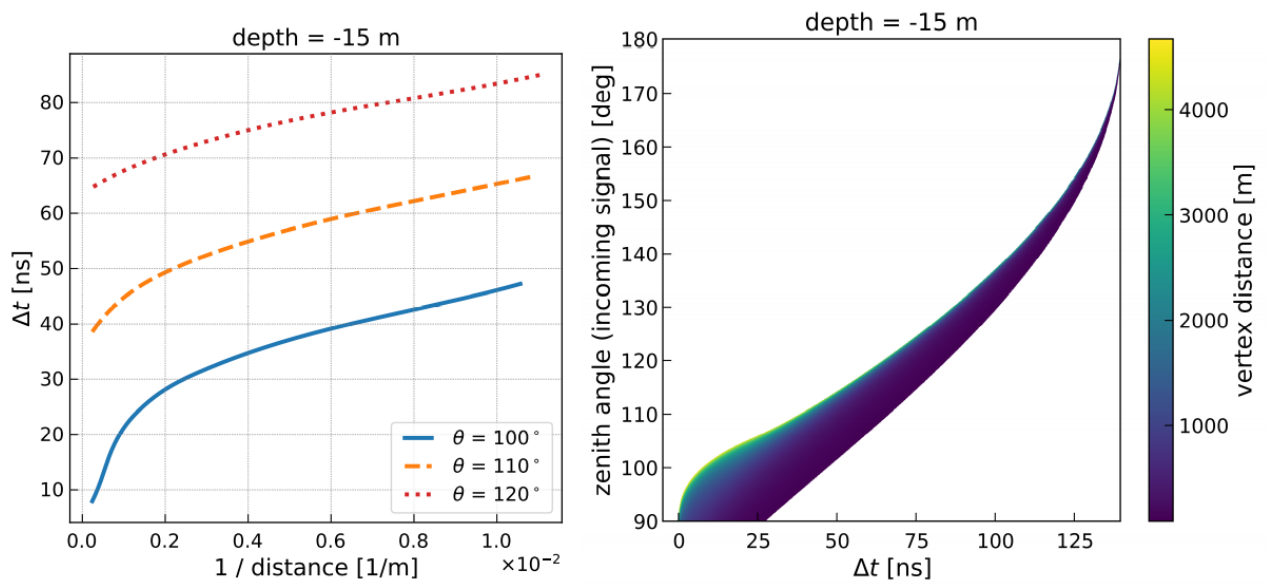


Figure 1.4: (left) Time delay between direct and reflected signal as a function of the inverse distance to the neutrino vertex, for three incoming signal directions. (right) Distance to the neutrino vertex (color coded) as a function of the incoming signal direction and time delay. Figure and caption from [5]

Chapter 2

Snow Accumulation Measurement

As mentioned in Sec. 1.4, for the precise reconstruction of the neutrino energy and direction a proper knowledge of the snow accumulation as well as the index-of-refraction profile is indispensable. Two different (a classical and deep learning) analyses of snow accumulation data from the ARIANNA station 52, equipped with an periodically triggered emitter, are presented in Sec. 2.1 and 2.2. In the former, an analysis procedure that was first presented in [5] is repeated on an expanded dataset of 14 months.

2.1 Classical Analysis

For this purpose station 52 of the ARIANNA detector array was supplemented with a dipole antenna 40 m away and 18.2 m deep, used as a periodically-triggered emitter to reconstruct the snow height at this station in real time (see Fig. 2.1). In this analysis the recorded trace from the deep dipole antenna 8.6 m below the surface is used since the time delay for the shallow LPDA antennas is too small for reconstruction. 150 of these artificial radio emissions (called events, with a physical length of 265 ns each) are bundled together to a burst with a repetition rate of 0.5 Hz between two events, resulting in a duration of 5 minutes [5]. This measurement is presently ongoing with a burst every 12 hours. In this analysis 14 months of data from the 7th of December 2018 to the 11th of February 2020 are presented. Though a burst always contains 150 events not all events can be transmitted via the long-range wifi system if weather conditions are bad. However, the first of each burst is always transferred using the Iridium satellite system.

Figure 2.2a shows an example of such an event, depicting the raw radio trace. An arbitrary temporal offset from event to event can be observed which has to be corrected for if one wants to average over all events in a burst. That is desirable since the signal goes with the number of events $\propto N$ whereas the noise scales only with $\propto \sqrt{N}$, effectively suppressing the noise and

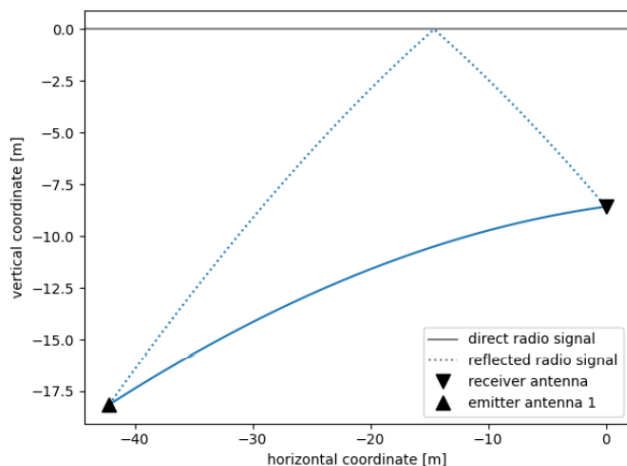


Figure 2.1: Sketch of a calibration station consisting of one emitter and receiver dipole antenna. The recorded signal has the D'n'R signature, composed of the early direct signal and the at the ice-air interface reflected signal. The timedelay between both signals relates to the snow accumulation.

thus making the computation of the time delay preciser.

In Fig. 2.2b, the averaged trace is shown in blue, complemented by the Hilbert envelope in orange. Subsequently a template of the direct pulse is created, by filtering the latter out and applying a Hanning window in the time domain, centred around the Hilbert maximum with a width of 6 ns and a rising (falling) flank of 3 ns. Once the template is obtained the direct pulse template (black, dashed line) is applied to the averaged trace to precisely determine the position of the direct pulse in the trace; that is the cross correlation being maximum. Afterwards, a phase shift of 57° and an attenuation given by the ratio in amplitude between direct and reflected $A_r/A_d = 1.43 - 1.61$ pulse of the Hilbert envelope is applied to the direct template. The phase shift and attenuation is applied according to the Fresnel equations for light at the interface between two different optical media. The reflected pulse template (black, dotted line) is slid over the initial, averaged trace in search for the optimal position of the reflected pulse. There are four bumps visible for which the following terms from left to right will be used henceforth: Direct and reflected pulse, 1st and 2nd afterpulse.

Figure 2.2c shows the cross correlation between the direct template (reflected template) and the averaged trace in blue (orange). The maximum in the former cross correlation directly corresponds to the optimal position of the direct pulse (marked by the dotted vertical line). When shifting the reflected pulse over the trace the overlap between the template and the direct pulse in the average trace causes a high maximum. However this is not the desired position, thus the next highest maximum is selected (marked by the dashed vertical line).

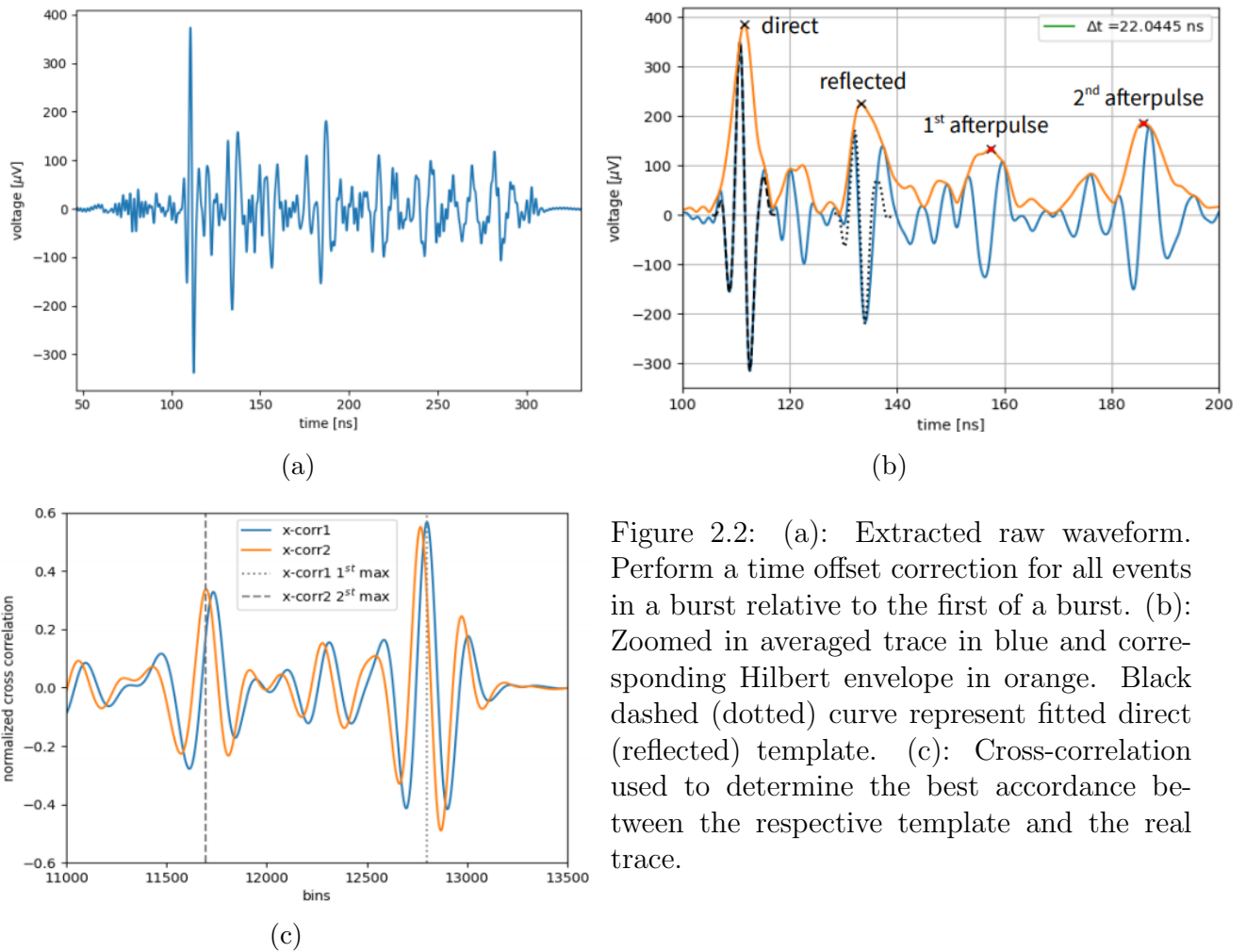


Figure 2.2: (a): Extracted raw waveform. Perform a time offset correction for all events in a burst relative to the first of a burst. (b): Zoomed in averaged trace in blue and corresponding Hilbert envelope in orange. Black dashed (dotted) curve represent fitted direct (reflected) template. (c): Cross-correlation used to determine the best accordance between the respective template and the real trace.

The procedure explained in the previous paragraph was applied to all available data within the acquisition period from the 7th of December 2018 to the 11th of February 2020 and is depicted in Fig. 2.3. The left scale represents the time difference between the direct and the reflected pulse in ns, while the right scale shows the corresponding snow accumulation in cm relative the first measurement. In this graph two types of data are plotted: First, the blue data point relate to the time difference from the averaged traces, while the orange band is obtain if the upper procedure is applied to each of the 150 individual events within a burst. Thus for each burst there is one blue dot (averaged trace over 150 individual traces) and 150 orange dots (individual traces).

During the Arctic winter break from mid-April to mid-September 2019 when the power shuts down at the station no events were recorded thus the lack of data within the period. In another period from mid-October to December 2019 only data from the first of each burst is present, which is linked to data transfer issues. This example shows that the analysis is robust enough to be performed on single events alone. The individual data is in good accordance with the averaged traces within the spread. However, as can be seen the width of the spread of the orange data increases with progressing data and growing snow height, especially after the winter break. This can be interpreted as artefacts of the analysis because increasing time delay means that the reflected pulse is detected later and finally interferes with the 1st afterpulse (see Fig. 2.2b) causing reconstruction difficulties. This seems only to affect the individual traces but not the average. Another feature are the steep rises in snow accumulation which coincide with the red vertical band that indicate high trigger rates. These rates are a proxy for a noisy background and appear when storms cause snow grains to scratch and trigger the antennas.

The nature of the afterpulses is yet not well understood but two hypothesis are under consideration. One is that the afterpulses are artefacts of the hardware used, namely the pulser and the antenna. Thus, the trigger signal that goes to the antenna could for example be reflected back and forth and trigger the antenna a second time after a time delay of about 45 ns. Unknown raytracing solutions, additional to the direct and reflected solutions described earlier, constitute another hypothesis and have been reported in previous works [7][8]. However, further study is required to understand the causes of these artefacts and to eliminate or suppress this effect.

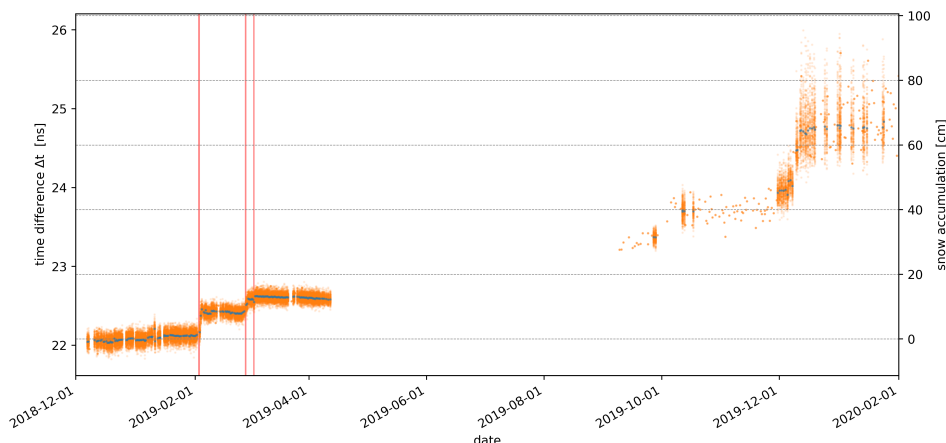


Figure 2.3: Time difference between direct and reflected pulse on the left over 14 month. The right scale plots the corresponding snow accumulation. During the Antarctic winter no signals are recorded due to power shortage. After roughly a year around 60 cm of snow has accumulated which is in accordance with geological experiences. Steep rises in the snow height correlate to high noise rates (vertical lines) detected independently at the station.

2.2 Deep Learning Analysis

As explained in the last section, analysis artefacts make the event-by-event reconstruction of the D'n'R time difference a complicated matter. At this point machine learning and in particular deep learning algorithms and neural networks come into play. Their strength is finding patterns in the data and to generalise these patterns to common rules. Thus, a deep learning analysis has the potential to perform better than classical analysis tools because it makes use of structure that the traditional programmer is unaware of. In this study data samples are generated for the supervised training of a convolutional neural network for purpose of regression. The performance of the network on a testing dataset is evaluated to modify the architecture and other key parameters of the network.

For the simulation of a dataset used for training, validating and testing a template of the direct pulse was cut out and used in the construction of an artificial radio trace. The template was then phase shifted and attenuated according to Sec. 2.1 to obtain the reflected one. Subsequently the templates are arranged apart by a random time difference between 5 ns to 30 ns (see Fig. 2.5), that will be used by the neural network as a label. All traces have a duration of 500 ns which corresponds to 2500 bins for a 0.2 ns resolution. In order to make the dataset more realistic, thermal noise was added and specific parameters (temporal offset of the direct pulse relative to start, time delay between the direct and reflected pulse, phase shift and attenuation of the reflected pulse and amplitude of the direct pulse) were varied according to a uniform distribution with set boundaries. So far no afterpulses were included in the generation of the training dataset. Different datasets were generated with various size ranging from 10^4 to 10^6 traces.

Figure 2.4 shows the architecture of a very simple neural network consisting of four 1D-convolutional layers that are flattened and then compacted by a dense layer to a single number, that is the time difference of the D'n'R pulse. Training for this simple network, which has 352,545 trainable parameters takes about 20 minutes on a GPU server. Results are shown in Fig. 2.6: The left plot depicts the loss function for the training (blue) and validation dataset (orange). A steep fall is observable within the first epochs. On the upper panel to the right the reconstructed over the true time difference is plotted, while in the lower panel the residuals between true and reconstructed are plotted. Ideally this would be a straight, horizontal line at zero, but since the reconstruction is not perfect deviations from the true value appear. This is best visible at the boundaries of data range where deviations are strong. For small ΔT s the network seems to overestimate while at large ΔT s it over- as well as underestimates. This is a well known issue in the training of neural networks and is caused by the relatively small number of events at the limits of the training dataset. In this case events with delays between 5 ns to 30 ns were simulated. If the performance of the network was to be improved in the low ΔT region one would simply have to reduce the lower bound to 3 ns for example.

However, further work is needed to find the optimal architecture and model parameters that reconstruct the D'n'R time difference with highest precision before the network can be applied to the real data presented in Sec. 2.1. It remains to be seen how well the simulated data compares to real data and if the network is robust enough to be performed on traces featuring artefacts such as afterpulses.

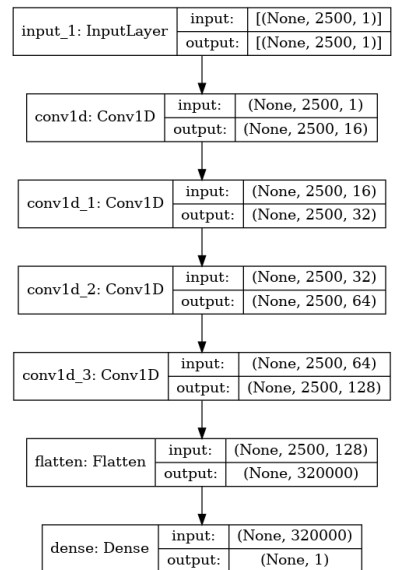


Figure 2.4: Architecture of the neural network consisting of a series four convolutional and seperable convolutional layers followed by a dense layer.

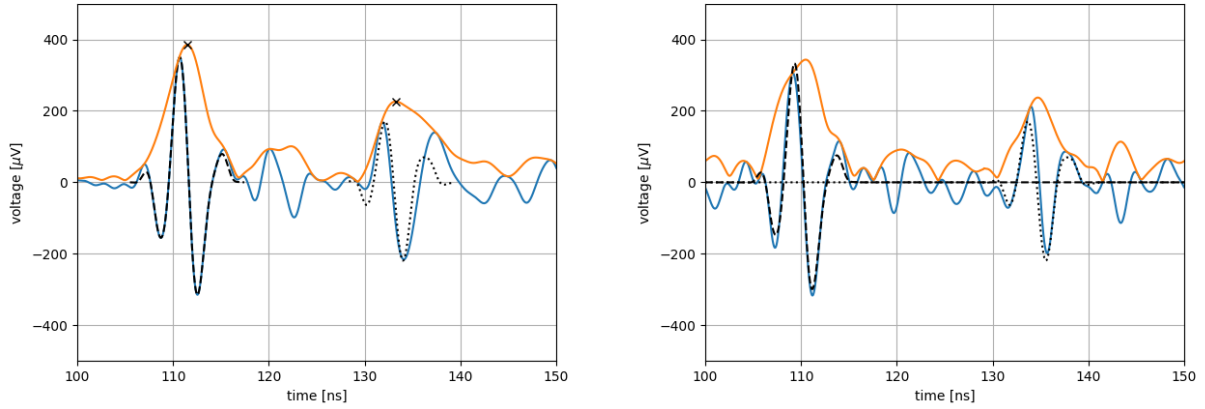


Figure 2.5: (left) Example trace of a real event. (right) Simulated event following the procedure mentioned in the text.

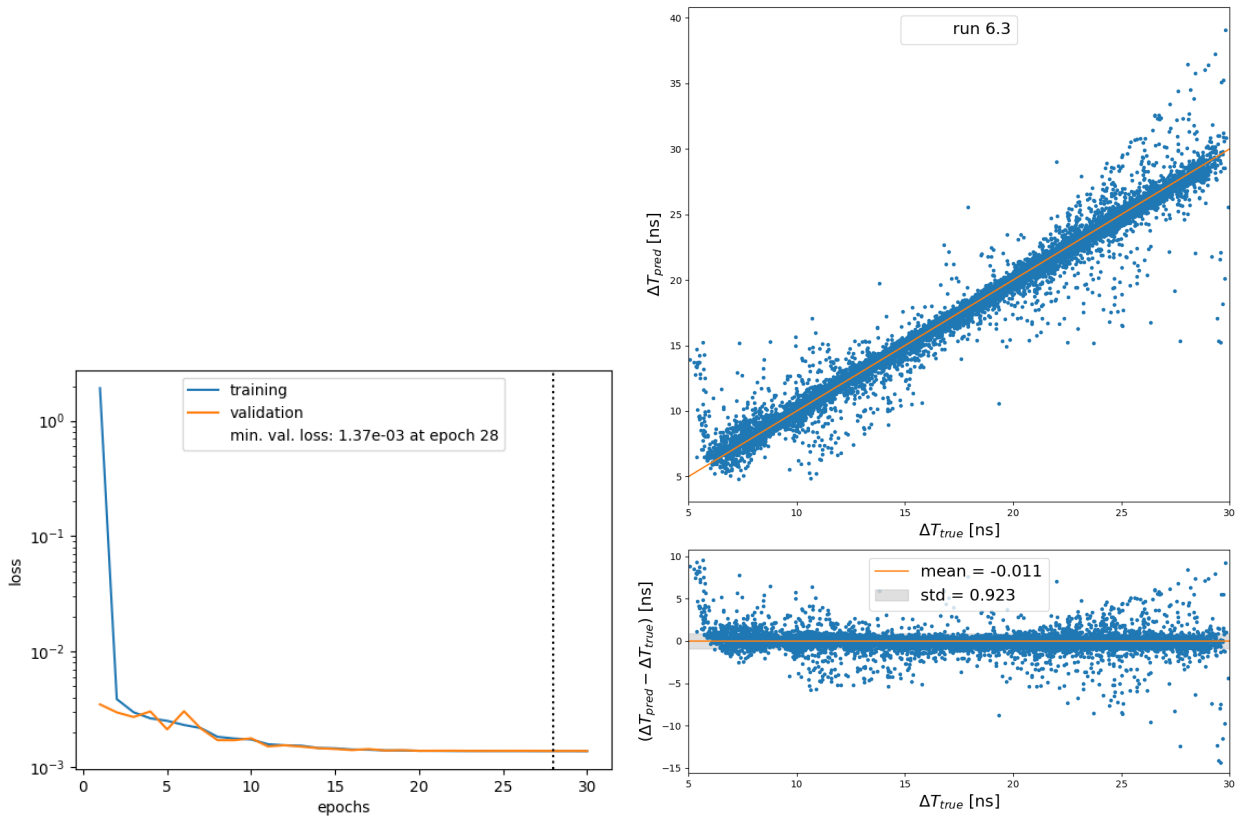


Figure 2.6: (left) Loss function over the number of epochs. In the case of run6.3 the minimum value of $1.37 \cdot 10^{-3}$ is reached at epoch 28. The blue line shows the loss of the training set while the orange line represents the validation loss. (right) Performance of the neural network on the test dataset shown as the reconstructed over the true time differences. A fit through the residuals yields -0.011 ± 0.923 .

Chapter 3

Simulation of a Detector Extension for the Measurement of Firn Properties

As discussed in Sec. 1.4 the snow accumulation and index-of-refraction profile are crucial parameters for the neutrino energy and direction reconstruction. A calibration device monitoring the snow accumulation at the Ross Ice Shelf and the analysis 14 month of data were presented in Chap. 2. This chapter aims to simulate an in-situ calibration device as extension to the current detector setup capable of additionally reconstructing the firn properties. This is of special interest for a shallow station design since the index-of-refraction profile varies greatly within the first 100 m. The optimal combination of emitter antennas is investigated and the achievable precision is quantified.

3.1 Concept

The parameters of interest for the study are the snow accumulation h and the index-of-refraction profile $n(z)$ as a function of the depth z which is defined by an exponential function

$$n(z) = n_0 - \Delta n \cdot \exp -z/z_0,$$

in which $n_0 = 1.78$ is the refractive index of the deep ice that was determined in borehole measurements. The change of refractive index Δn and the attenuation length z_0 are subject to greater measurement uncertainty and must therefore be determined in-situ by the calibration device. Thus the three parameters to be reconstructed by the calibration are h , Δn and z_0 .

In order to fit three independent parameters at least three observables are required. Using only one emitter from which only one D'n'R difference can be obtained would not suffice, thus a second emitter antenna is necessary (see Fig. 3.1). For a given antenna configuration the raytracing algorithm is performed and the propagation times are obtained taking $h = 0$ m, $\Delta n = 0.46$, $z_0 = 34.5$ m as input parameters. Since only relative time differences are of interest the four propagation times are converted into

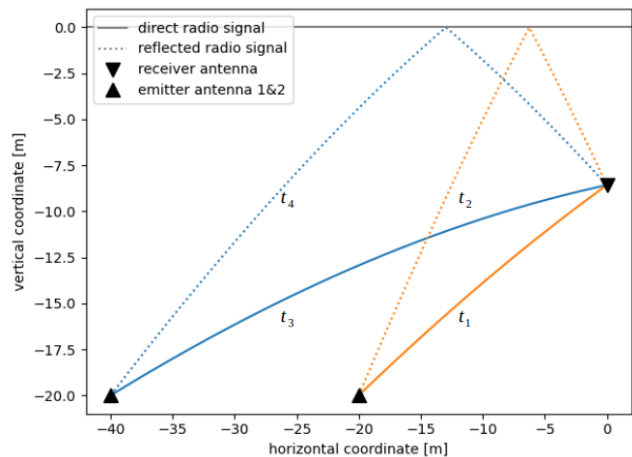


Figure 3.1: Sketch of a calibration station consisting of two emitters and one receiver capable of measuring the snow accumulation and the index-of-refraction profile at the same time from the D'n'R signature alone.

the three observables

$$\Delta T_1 = T_2 - T_1, \quad \Delta T_2 = T_3 - T_1, \quad \Delta T_3 = T_4 - T_1.$$

In order to simulate a real detection that underlies statistical fluctuations and hardware limitations in the time resolution, the propagation times are smeared 100 times according to a Gaussian distribution of 0.2 ns. The resulting 300 observables are fitted at ones to receive the reconstructed values of h , Δn , z_0 (see Fig. 3.2).

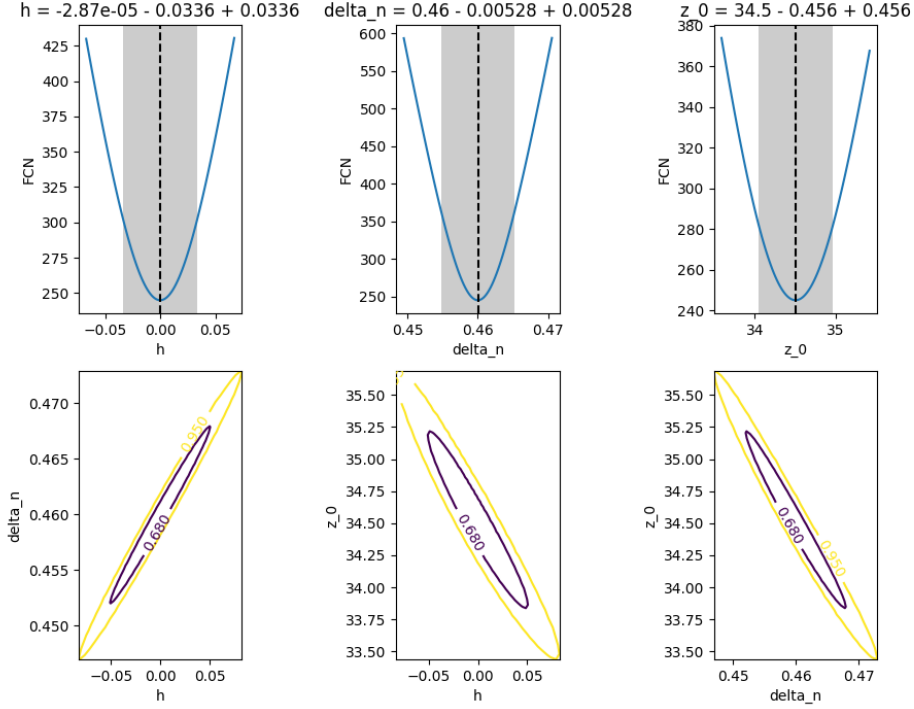


Figure 3.2: Fit of h , Δn , z_0 for a specific E1-E2 configuration. The upper panel shows the χ^2 profile while the lower panel depicts correlation between the parameters. As can be seen h and Δn strongly correlate while h and z_0 , as well as Δn and z_0 strongly anti-correlate.

Having the position of two emitters and one receiver antenna as open parameters allows for many different configurations. Since the receiver antenna position is also constrained by the neutrino energy reconstruction the variation of this position is not considered in the study. For the two remaining emitters (emitter 1 = E1, emitter 2 = E2) one has to come up with a systematic way of testing all possible combinations. Therefore a grid in the x-z plane of width 5 m by 5 m, restrained by the condition of having exactly two raytracing solution (direct and reflected) and high efficiency in the total-internal reflection at the surface, is used. Fixing E1 at the first position, E2 probes all remaining position on the grid. This was done in Fig. 3.3 left where E1 is indicated by the red star while the coloured squares symbolise the combined reconstruction resolution for E2 at the respective positions. This value combines the reconstructed uncertainty in h , Δn , z_0 that is $\sigma(h)$, $\sigma(\Delta n)$, $\sigma(z_0)$

$$\sigma_{comb} = \sqrt{(\sigma(h)/1 \text{ cm})^2 + (\sigma(\Delta n)/0.0046)^2 + (\sigma(z_0)/34.5 \text{ cm})^2},$$

since the optimal position should be a compromise on the reconstruction resolution between the three parameters.

The minimal value at position 82 of the reconstruction resolution, for E1 fixed at position one, is marked by a red circle. The pair of E1 (red star) and the corresponding optimal position of E2 (red circle) is used in the next step. Due to the interchangeability of E1 and E2 the number of computations are halved. For example, if E1 is fixed at the very first position and the reconstruction resolution for E2 at the second position is determined, than the combination of E1 at position two and E2 at position one should yield the same result within the statistical uncertainties, because only the labels were swapped. Figure 3.3 right shows E1 at the final position of the grid with the optimal position of E2 at 48.

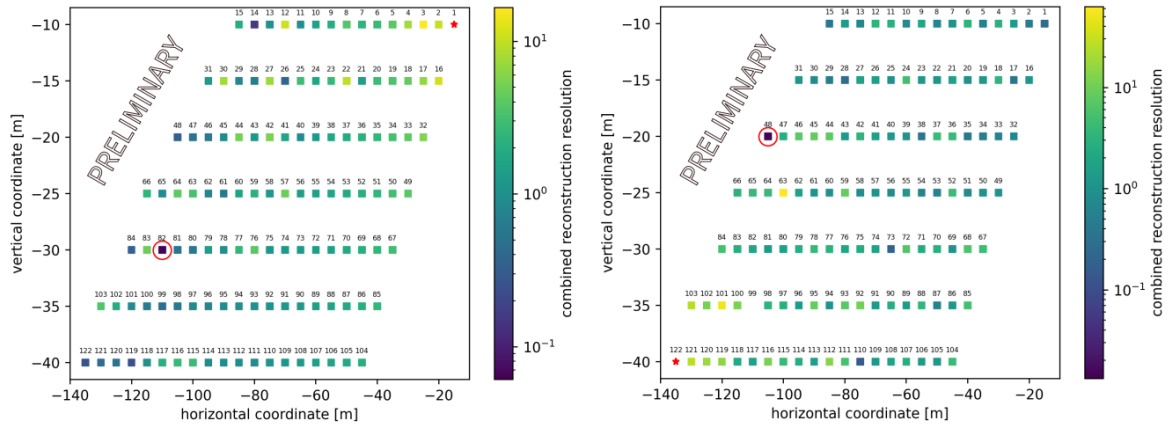


Figure 3.3: Scan of position of E2 over the grid for a fixed position of E1. For each emitter configuration the raytracing solution is determined and a measurement simulated by smearing the propagation times with a Gaussian distribution and fitting the parameters h , Δn and z_0 . On the left, E1 was fixed at position one, while on the right E1 was fixed to the last position on the grid, 122. The x and y-axis depict the spatial position (x and z) of the emitter antennas while the color scheme represent the combined reconstruction resolution. The smallest value in the grid is then passed on the next stage in which results from all E1 positions are compared.

3.2 Results

If the procedure shown in Fig. 3.3 is repeated over the entire grid of possible E1 positions one ends up with Fig. 3.4 which shows for fixed E1 at the upper index position the optimal position of E2 is at the lower index. The color scheme displays the minimum combined reconstruction resolution. The optimized, overall configuration of E1 and E2 is indicated by red circles. It turns out that E1 at position 102 and E2 at position 107 (and vice versa) return the lowest value of the combined reconstruction resolution of $< 10^{-4}$ that can be transformed into the corresponding uncertainty $\sigma(h)$, $\sigma(\Delta n)$, $\sigma(z_0)$. These results are preliminary since the simulation has to be tested for existing inconsistencies and reproducibility.

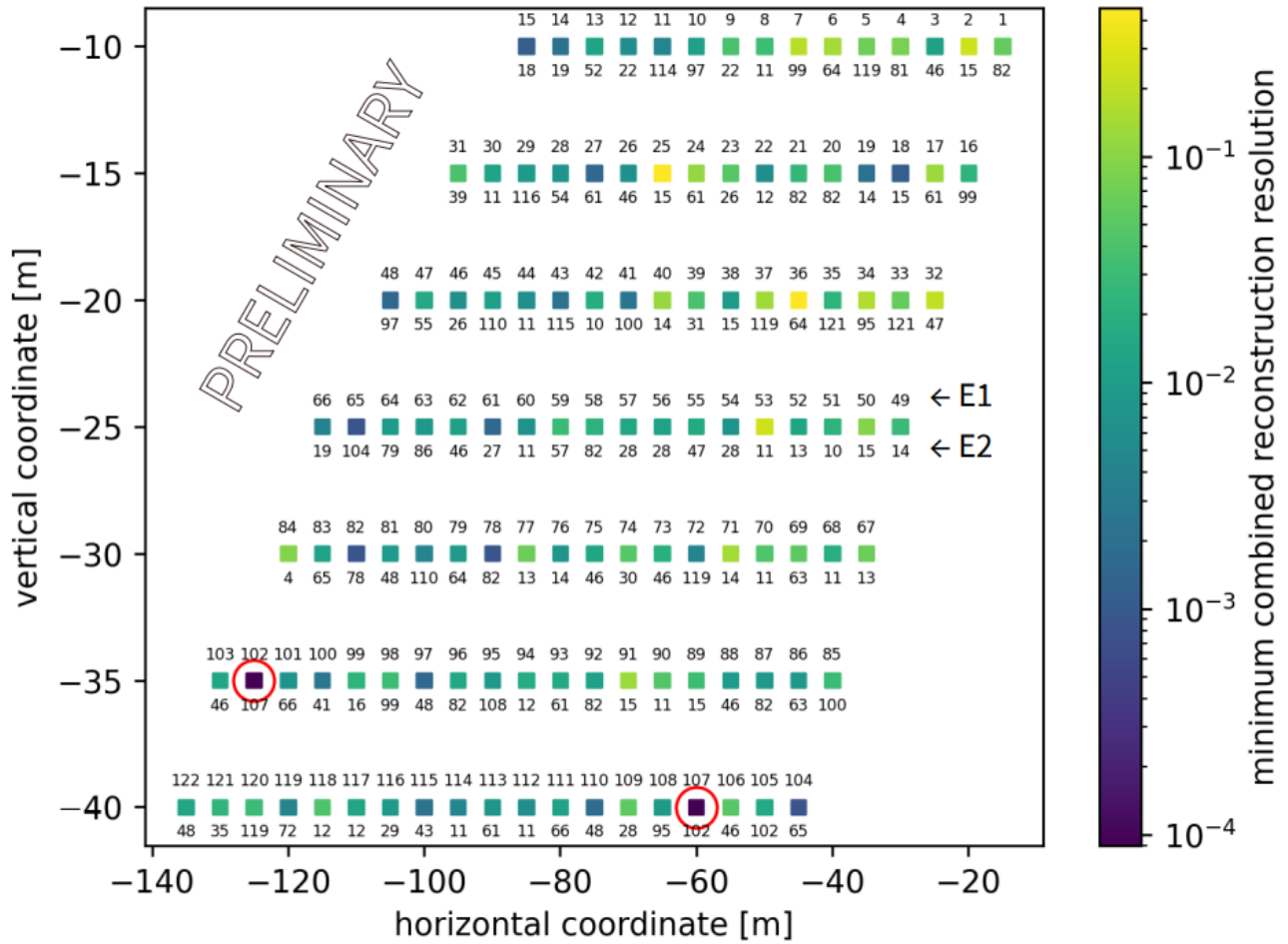


Figure 3.4: Each dot in the grid corresponds to the optimum position of E2 if E1 is fixed to the position indicated by the upper index. The position of E2 can be read of from the lower index. The color code symbolises the value of the minimum combined reconstruction resolution. The red circled positions correspond to the emitter pair for which the minimum value over the entire grid is obtained.

Chapter 4

Summary and Outlook

In this half time report of my master thesis an introduction to neutrino detectors in general and in particular radio neutrino detectors was given. For a particular detector, the ARIANNA radio array, a detailed description of the experimental station design and neutrino energy reconstruction was presented. In a next step, first results of snow accumulation data from station 52 of the ARIANNA detector were independently analysed, constituting in a confirmation of the existing analysis performed on 4 month of data and expanding the data period to 14 month between December 2018 to February 2020. This is a success for the relatively new D'n'R technique and shows the reliability of the method. Artefacts within the analysis were studied but further work is needed to conclude on the origin of the anomalies and to compensate or eliminate the effects.

In a different approach to extract the D'n'R time differences from the radio traces, a deep learning algorithm was modelled and training data was simulated. This project requires further study to optimise the architecture of the neural network and to subsequently apply the model on real data. It remains to be seen how close the simulated data comes to real data and how robust the algorithm is against variations of that type.

Furthermore, this work presents a simulation study for an in-situ calibration device capable of reconstructing the snow accumulation as well as the firm properties which are crucial for the neutrino energy reconstruction. The results are so far preliminary since remaining inconsistencies have to be understood and the reproducibility has to be ensured. However, a finalised proposal for the ice-calibration design is just around the corner.

In the successive, second part of my two semester master thesis I aim to continue to work on the open matters mentioned above and to deepen my skills regarding deep learning algorithm, by expanding the scope of the neural network project to the reconstruction of the vertex distance from the D'n'R pulse based on full Monte Carlo neutrino event simulations.

References

- [1] Gen2 Collaboration et al. *IceCube-Gen2: The Window to the Extreme Universe*. 2020. arXiv: 2008.04323 [astro-ph.HE].
- [2] Maurizio Spurio. *Particles and Astroparticles*. Heidelberg: Springer, 2015.
- [3] Gurgen A. Askaryan. “Excess negative charge of an electron-photon shower and its coherent radio emission”. In: *Soviet Physics JETP* 14.2 (1962).
- [4] A. Anker et al. “Targeting ultra-high energy neutrinos with the ARIANNA experiment”. In: *Advances in Space Research* 64.12 (Dec. 2019), pp. 2595–2609. ISSN: 0273-1177. DOI: 10.1016/j.asr.2019.06.016. URL: <http://dx.doi.org/10.1016/j.asr.2019.06.016>.
- [5] A. Anker et al. “Neutrino vertex reconstruction with in-ice radio detectors using surface reflections and implications for the neutrino energy resolution”. In: *Journal of Cosmology and Astroparticle Physics* 2019.11 (Nov. 2019). ISSN: 1475-7516. DOI: 10.1088/1475-7516/2019/11/030. URL: <http://dx.doi.org/10.1088/1475-7516/2019/11/030>.
- [6] C. Glaser et al. “NuRadioMC: simulating the radio emission of neutrinos from interaction to detector”. In: *The European Physical Journal C* 80.2 (Jan. 2020). ISSN: 1434-6052. DOI: 10.1140/epjc/s10052-020-7612-8. URL: <http://dx.doi.org/10.1140/epjc/s10052-020-7612-8>.
- [7] C. Deaconu et al. “Measurements and modeling of near-surface radio propagation in glacial ice and implications for neutrino experiments”. In: *Physical Review D* 98.4 (Aug. 2018). ISSN: 2470-0029. DOI: 10.1103/physrevd.98.043010. URL: <http://dx.doi.org/10.1103/PhysRevD.98.043010>.
- [8] S.W. Barwick et al. “Observation of classically ‘forbidden’ electromagnetic wave propagation and implications for neutrino detection.” In: *Journal of Cosmology and Astroparticle Physics* 2018.07 (July 2018), pp. 055–055. ISSN: 1475-7516. DOI: 10.1088/1475-7516/2018/07/055. URL: <http://dx.doi.org/10.1088/1475-7516/2018/07/055>.